ADVANCED MATERIALS INTERFACES
www.advmatinterfaces.de

Assessment of Pressure and Density of Confined Water in Graphene Liquid Cells

Seyed Mohammadreza Ghodsi, Seyyed Soroosh Sharifi-Asl, Pavel Rehak, Petr Král, Constantine M. Megaridis,* Reza Shahbazian-Yassar,* and Tolou Shokuhfar**

Understanding the behavior of confined matter within Van der Waals (VdW) materials is complicated due to the interplay of various factors, including the VdW interaction between the interlayers, the layer interaction with the matter, and the bending strain energy of the layers to accommodate encapsulation. Herein, new insight on the magnitude of pressure and density of water entrapped within confined spaces in VdW materials is provided. This is accomplished by studying the plasmon excitation of water encapsulated between two sheets of graphene membranes in an aberration-corrected scanning transmission electron microscope. The results indicate ≈12% maximum increase in the density of water under tight graphene encasement, where pressure as high as 400 MPa is expected. The pressure estimation from theoretical analysis considering the effect of VdW forces, Laplace pressure, and strain energy is in agreement with the experimental results. The findings of this work open new opportunities to explore the local physical state of not only water but also other liquid materials under high pressure with imaging and analytical resolutions never achieved before.

1. Introduction

Encasement of nanometer-thick films of liquids in Van der Waals (VdW) materials is believed to deviate the behavior of confined matter from bulk.[1–6] This configuration provides a novel platform to perform fundamental thermodynamic studies on liquid solutions under such confinement.[7] In a closely-confined system, VdW forces are inversely proportional to the scale of confinement and act more strongly as the thickness of the entrapped liquid film declines.[4] Moreover, the energy cost of bending a 2D membrane over the confined sample should be considered, since the VdW forces and bending strain energies are expected to impose substantial pressure on the entrapped liquid. The escalation of pressure in liquids under confinement has been confirmed by the appearance of confined water (trapped between hydrophobic graphene membranes) as ice at room temperature.[8] While this observation has also been supported by molecular simulations,[9–13] there have been further experimental efforts to understand the effect of pressure on confined liquids. Infrared (IR) spectroscopy detected the transformation of $MgCl_2$ crystals to MgO in water upon encapsulation between graphene sheets.[14] Giving the chemical neutrality of saturated carbon bonds in graphene and the negligible interference of IR beam with the sample, the reaction was solely contributed to the tight confinement effects on $MgCl_2$ suspension. Likewise, the polymerization of buckminsterfullerene (C60) has been observed under graphene entrapment, a reaction which is not thermodynamically feasible under ambient conditions.[15] In yet a different set of experiments, atomic force microscopy (AFM) has been used to directly measure the pressure of confined water, where pressures as high as 1 GPa were reported.[16]

The advent of graphene liquid cell (GLC) transmission electron microscopy (TEM) has enabled the study of water and liquid solutions with unprecedented spatial and analytical resolutions.[17–19] Specimens contained within layers of graphene have negligible interference with the electron beam[20–22] and minimize the scattering of transmitted electrons required for high resolution imaging and spectroscopy. In addition,

Dr. S. M. Ghodsi, Prof. T. Shokuhfar
Department of Bioengineering
University of Illinois at Chicago
Chicago, IL 60607, United States
E-mail: tolou@uic.edu

Dr. S. S. Sharifi-Asl, Prof. C. M. Megaridis, Prof. R. Shahbazian-Yassar
Department of Mechanical and Industrial Engineering
University of Illinois at Chicago
Chicago, IL 60607, United States
E-mail: cmm@uic.edu; rsyassar@uic.edu

P. Rehak, Prof. P. Král
Department of Chemistry
University of Illinois at Chicago
Chicago, IL 60607, United States
E-mail: pkral@uic.edu

Prof. P. Král
Departments of Physics
Biopharmaceutical Sciences
and Chemical Engineering
University of Illinois at Chicago
Chicago, IL 60607, United States

The ORCID identification number(s) for the author(s) of this article can be found under https://doi.org/10.1002/admi.201901727.

DOI: 10.1002/admi.201901727

graphene has excellent flexibility[23] and impermeability toward molecules as small as water, which makes it an ideal substrate for in situ TEM study of liquid samples.[21,24,25] Wang et al.[26] have exploited GLC–TEM capabilities to study the state of iron oxide cores of hydrated ferritin protein shells via electron energy-loss spectroscopy (EELS). Moreover, EELS has been applied on the GLC of TiO_2 nanoparticles in the presence of cell-culture media to study the dynamics of protein corona formation on nanoparticles.[27] In yet more relevant work, the structure of water molecules was examined using GLC–TEM where the formation of square ice at room temperature under tight graphene encasement was reported.[9,17,28–30] These reports, along with many others on the application of EELS and TEM or scanning TEM (STEM) on graphene-encased wet samples,[31,32] have shown the feasibility of GLC–TEM to observe and analyze liquids with unprecedented spatial and energy resolution.

While the existence of high pressure in liquid solutions under graphene confinement has been reported,[7] the magnitude of the pressure is still under investigation. Moreover, previous studies have utilized nontransmission probes, including AFM, Raman, and Fourier-transform infrared (FT-IR) spectroscopy, to examine the liquid samples confined between VdW materials and atomically-smooth substrates like *h*BN and MoS_2,[7,16] but there are no previous reports on the thermodynamic state of liquids confined solely between VdW material interlayers. The relatively small size of graphene liquid pockets in GLC compared to the spatial resolution and probe size of conventional analytical methods constrains the application of common nontransmission spectroscopy tools in studying such confined samples. Recent developments in two-dimensional materials synthesis[33] and the advent of aberration-corrected electron microscopy[34] have opened new opportunities to explore confined liquids within graphene substrates with unprecedented spatial–energy resolutions. Herein, we report a detailed theoretical and spectroscopic analysis on the density and pressure of water encapsulated in GLCs. Particularly, the plasmon and valence excitations of graphene-encased liquids are used to estimate the pressure exerted on liquid pockets between graphene sheets. Our experimental results indicate a 12% elevation in the density of graphene-entrapped water where pressures as high as 400 MPa are reached at room temperatures. Furthermore, our energy conservation analysis and simulations of GLCs considering the effect of VdW forces, Laplace pressure, and strain energy is in agreement with the experimental results.

2. Low-Loss EELS Analysis of Graphene-Encapsulated Water

Considering that EELS is widely used in (S)TEM experiments to study the composition and local electrical structure of specimens with high spatial and analytical resolution,[35] we studied the behavior of GLC-encased water low-loss EELS data. **Figure 1** demonstrates the STEM and EELS results of water confined within a GLC. Figure 1a illustrates a GLC where layers of graphene on top and bottom encase a film of water. Figure 1b depicts the dark-field STEM micrograph of a GLC where the dashed lines represent the GLC boundary. The dark gray area surrounding each GLC consists of dry graphene layers. The bright spot in the bottom right corner of the image is believed to be copper remnant on the outer surface of graphene from the GLC fabrication procedure (Figure S1, Supporting Information).[36] The absence of copper and/or salt contaminations in the sampling area was confirmed by acquiring EELS core-loss signal across the sample (Figure S2, Supporting Information). The low-loss EELS spectra of empty cell (dry graphene layers) and GLC (graphene layers + water) shown in Figure 1c were acquired separately from the designated colored spots in Figure 1b. The thickness index of the GLC (t_{max}/λ) is derived from its EELS low-loss spectrum, where t_{max} is the thickness of the GLC and λ is the inelastic mean free path of electrons in the sample. The low-loss EELS signal of dry graphene layers in this sample has a low-loss plasmon peak located around 23 eV. Previous studies have shown that the plasmon peak position of graphene sheet is a function of its number of interlayers.[37] The reported plasmon peak position of single/double graphene layers has been estimated to be around 15 eV,[38] and increasing upon the addition of more graphene layers.[39] Although finding the exact number of graphene layers in the GLC is a tedious task, the EELS acquiring spots were chosen closely enough to safely assume that the number of graphene layers in dry and wet regions are identical in each GLC system. The isolated water signal was attained by subtracting the normalized dry graphene signal from that of the GLC (Figure 1d). The exact position of the plasmon peak was determined by fitting a Gaussian distribution to the subtracted peaks (Figure S3, Supporting Information). Interestingly enough, the isolated plasmon peak of water, when trapped between graphene layers in this particular GLC system, is positioned at 22.34 ± 0.11 eV. This is distinct from the plasmon peak of water in a liquid flow holder (20.99 ± 0.18 eV), where water with much larger thickness (≈1 µm) is contained between two silicon nitride (Si_3N_4) membranes (Figure S4, Supporting Information). Considering previous studies where the pressure of water entrapped between Si_3N_4 membranes in a liquid flow holder was shown to be atmospheric,[40] it is safe to assume that 1 µm thick water layer in the flow holder apparatus has physical properties identical to those of bulk water.

The plasmon peak of a GLC is a function of its composition, thickness, and pressure. Even though water and graphene are the sole constituents of each GLC, the variation in number of graphene interlayers along with the thickness of the encapsulated water film will shift the plasmon peak position in each GLC. Thus, it is crucial to repeat the EELS measurements on different GLCs with distinct geometries, graphene interlayer numbers, and thickness indexes (t_{max}/λ) to ensure the reproducibility of this method. While Figure 1 shows one of the examined GLCs, the measurements were repeated on two more GLCs, with multiple EELS acquiring spots on each GLC. The detailed results are presented in Figures S5 and S6, Supporting Information. The distinction between dry and wet spots in each case was confirmed by looking at the oxygen core-loss of the graphene/water system (Figure S7, Supporting Information). The energy resolution constraint of EELS (Figure S8, Supporting Information) along with the systematic errors induced in the process of isolating and fitting water signals, brings about

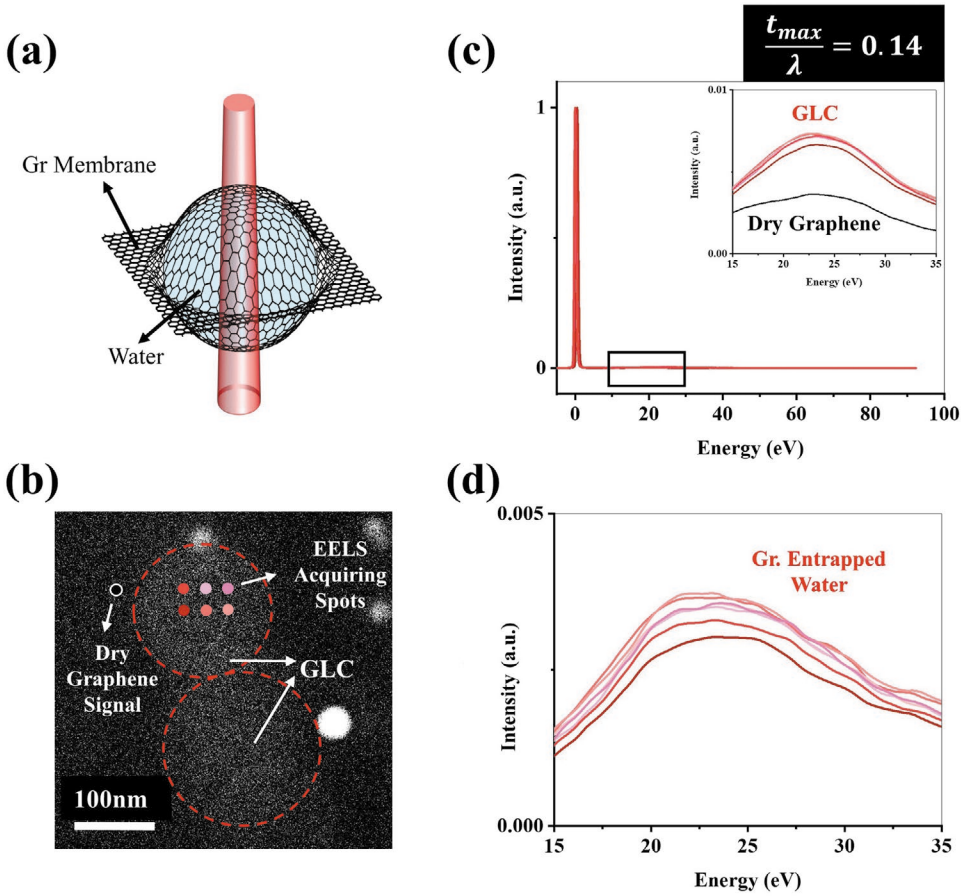

Figure 1. Scanning transmission electron microscopy (STEM) and electron energy-loss spectroscopy (EELS) results of water in a graphene liquid cell (GLC). a) Schematic of a GLC. The electron beam (red) passes through the GLC and is collected by a Gatan imaging filter (GIF) camera. b) Dark-field STEM snapshot of water GLC with thickness index (t_{max}/λ) of 0.14. A thin film of water is contained between graphene layers. The wet and dry regions in the GLC have been marked. EELS was performed on six consecutive spots in the GLC area, while the dry-graphene sheet signal was acquired in the designated dry-graphene region. c) Low-loss spectra of dry graphene layers (black line) and six spots on the water-encapsulated GLC (colored lines). The GLC is relatively thicker than dry graphene layers, which results in intensified scattering events and accentuated plasmon peak intensity. d) Isolated low-loss spectrum of water. By subtracting the dry signal from the wet signal curves in (c), the isolated low-loss spectrum of water was attained. The plasmon peak position of water in this specific GLC was 22.34 ± 0.11 eV.

uncertainties which are shown by the standard deviation of different measurements on each GLC.

3. Correlation Between EELS Plasmon Peak of Water and Its Density

Plasmons in the low-loss regime reflect the interactions of the electron beam with loosely bound electrons in the valence–conduction band.[41–43] According to the free electron model introduced by Egerton,[41] the wave-like oscillation of these electrons in contact with the electron beam is described by:

$$E_P = \frac{h}{2\pi}\omega_P \tag{1}$$

where ω_P is the oscillation frequency of plasmons, E_P the plasmon peak position, and h is Planck's constant.[44] While the intensity of plasmon peak is a function of water thickness, its position is invariant. Replacing the ω_P in Equation (1), we deduce:

$$E_p = \frac{\hbar}{2\pi}\sqrt{\frac{ne^2}{\varepsilon_0 m_e}} \tag{2}$$

where n is the number density of free electrons in the specimen, e the electric charge of an electron, m_e the approximate resting mass of electrons, and ε_0 is the permittivity of free space. While the components of this equation are independent of the specimen, n changes with the specimen composition, temperature, and pressure.[39] Comparing the isolated plasmon peak positions of nonconfined water (Figure S4, Supporting Information) and GLC (Figure 1), it is evident that the position of the plasmon peak has shifted toward higher energy values in the GLC. The acceleration energy of the electron beam, 200 keV, is significantly higher than the Fermi energy threshold, thus even nonbonding electrons participate in propagating plasmon oscillations.[44] In the simple free electron theory, where valence electrons move freely in the sample,[41] higher plasmon energy (E_p) values result from an increase in the density of valence electrons (n) in the sample:[44]

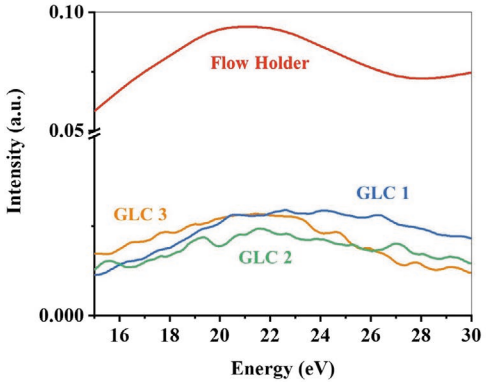

Sample	$\frac{t_{max}}{\lambda}$	Plasmon Peak Position (eV)	Water Density ($\frac{g}{cm^3}$)
GLC 1	0.14	22.34 ± 0.11	1.12 ± 0.10
GLC 2	0.27	21.61 ± 0.32	1.05 ± 0.03
GLC 3	0.35	21.51 ± 0.16	1.04 ± 0.02
Flow Holder	>1	20.99 ± 0.18	0.99*

Figure 2. The plasmon peak position of water in three graphene liquid cells (GLCs) and the Si-based liquid flow-holder. $\frac{t_{max}}{\lambda}$ is reported as an index of the GLC thickness, where larger values indicate thicker water film. The plasmon peak position shifts to higher values as the thickness of the GLC declines, indicating an elevation in the density of confined water. The density of water in the liquid flow-holder was assumed 0.99 g cm^{-3} with E_p fixed at 20.99 eV.

$$n_f = AE_{p,f}^2 \tag{3}$$

$$n_g = AE_{p,g}^2 \tag{4}$$

where n_f, $E_{P,f}$ and n_g, $E_{P,g}$ are the free-electron density and plasmon peak positions in the bulk and GLC-entrapped water, respectively, and $A = \frac{4\pi^2\varepsilon_0 m_e}{\hbar^2 e^2}$ is a constant. On the other hand, n is correlated to the density of water:

$$n_f = N_A \left(\frac{Z\rho_f}{M_W}\right)_{water} \tag{5}$$

$$n_g = N_A \left(\frac{Z\rho_g}{M_W}\right)_{water} \tag{6}$$

where N_A is Avogadro's number, M_W the water molecular weight, Z is the number of water free electrons, ρ_f and ρ_g are the bulk densities of water in the flow holder and GLC, respectively. Thus:

$$\rho = \frac{A M_W E_p^2}{Z N_A} \tag{7}$$

$$\rho_g = \rho_f \left(\frac{E_{p,g}}{E_{p,f}}\right)^2 \tag{8}$$

Figure 2 depicts the plasmon peak position of water in three GLC samples along with that of water in the Si-based liquid flow-holder. t_{max}/λ of each GLC sample is measured and reported as an index of the GLC thickness. The density of water in each GLC is measured by replacing $E_{p,g}$ and $E_{p,f}$ in Equation 8. Although there are no previous reports on the density of water in the Si-based liquid flow-holder system, it has been shown that water in the flow holder is at atmospheric pressure and thus has a density close to that of bulk water (ρ_f = 0.99 g cm^{-3}).[40] As is evident from Figure 2, the density of water under graphene confinement is inversely proportional to the sample thickness and rises as t_{max}/λ declines. The density of water is a function of temperature and pressure. Neglecting the thermal effects of the electron beam on the sample,[45] the density of water in either system is solely a function of the pressure within the sample at room temperature.

4. Rise of Water Density with Pressure Escalation Inside GLCs

While the pressure of water in either liquid-flow holder or GLC cannot be derived directly from low-loss EELS, electron spectroscopy can estimate the relative density of water in GLC as discussed earlier. Using the equation of state (EOS) for water at room temperature, we derived the pressure exerted on water due to graphene encapsulation by taking into account the change of water density. Assuming that the density of water in the liquid-flow holder is close to that of water at ambient conditions (0.99 g cm^{-3} at 25 °C and 1 bar),[40,46] it was shown in the previous section that the density of water in this particular GLC is 1.12 ± 0.10 g cm^{-3}. In order to derive the pressure of water corresponding to this density, the Tumlirz–Tait EOS was applied:[47]

$$V = V_\infty + \frac{\lambda}{P_0 + P} \tag{9}$$

where V is the specific volume of water (cm^3 g^{-1}), P the pressure of water (bars), and:

$$\begin{aligned} \lambda &= 1788.316 + 21.550T - 0.469T^2 \\ P_0 &= 5918.499 + 58.052T - 1.125T^2 \\ V_\infty &= 0.698 - 0.743\times10^{-3}T + 0.370\times10^{-4}T^2 \end{aligned} \tag{10}$$

with T in Celsius, P_0 in bars, V_∞ in cm^3 g^{-1} and λ in bar cm^3 g^{-1}. Equation (10) is illustrated in **Figure 3** associating the pressure

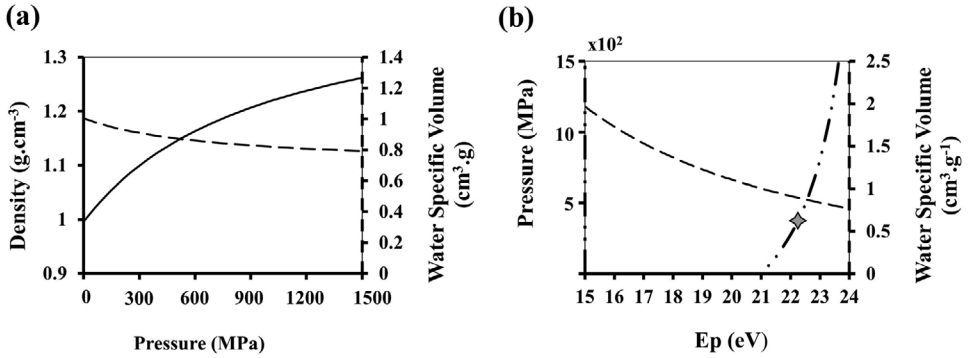

Figure 3. Pressure and density diagram of water. a) The Tumlirz–Tait correlation determines the density of water (solid curve) under a range of pressure values at 25 °C. The density of water increases as the pressure rises. The dashed line designates the correlation between the specific volume of water and its pressure at room temperature. b) Using Tumlirz–Tait's correlation along with plasmon frequency Equation (2), water pressure is plotted as a function of plasmon peak position (dot-dashed curve). The dashed curve shows the specific volume of water as a function of the plasmon peak position. The gray star on the graph designates the plasmon peak of water graphene liquid cell (GLC) located at 22.34 ± 0.11 eV, suggesting a GLC internal pressure value of 400 ± 50 MPa.

of water to its density (Figure 3a) and plasmon peak position (Figure 3b). The density of water increases while the specific volume of water decreases when the pressure escalates. Figure 2b was attained by correlating the pressure of water in Equation (9) to the density of water in Equation (7). The specific volume of water at ambient condition (25 °C, 1bar) was derived from Equation (9) (1.004 $cm^3\ g^{-1}$) and inserted into Equation (7) for $E_{p,f} = 20.99$ eV to calibrate the data set for Z. The specific volume of water in GLC is the inverse of its density and equals $0.89 \pm 0.07\ cm^3\ g^{-1}$. Figure 3b suggests such a tremendous change of V in water from bulk to GLC requires pressure rise of 400 ± 50 MPa. While the Tait equation of state has been reported to follow experimental data closely, it would be interesting for future studies to apply other well-known correlations including Stiffened Gas EOS or Noble-Abel Stiffened Gas EOS to estimate the pressure inside graphene bubbles.[48]

The possibility of such high pressures under graphene encapsulation agrees with some previously reported studies.[9,14,16] For instance, the AFM measurements and ab initio calculations on argon enclosures formed between layers of graphene and atomically-smooth Ir (100) wafer revealed internal pressure of Ar of the order of 5 GPa.[49] However, not all previous reports agree with the existence of such high pressure inside graphene enclosures. Khestanova et al.[16] reported pressures of the order of 10 MPa using the AFM-exerted force measurements on enclosures formed between graphene and Si–SiOx wafers. There have also been attempts to explain the pressure inside graphene-confined water using the Laplace pressure correlation, $\Delta P = \frac{2\gamma}{R}$ where ΔP is the pressure gradient across the graphene membrane, γ the interfacial energy of graphene–water and R is the radius of the graphene blisters.[50] Replacing $\gamma = 90$ mJ m^{-2} [51] and $R = 10$ nm, the internal pressure of GLCs could reach 18 MPa. The disagreement between our results and some other reports on the pressure of graphene enclosures is due to the fundamental differences between these systems.[16,50] In the GLC system, the hard supporting substrate is replaced by graphene layers to encase the sample. Moreover, the entrapped phase in a GLC is a liquid (mostly water), while in reported AFM measurements the specimen is a dilute inert gas. The GLC samples are also a few orders of magnitude thicker than gas cells, which signifies the role of graphene elasticity in the total pressure. Thus, the Laplace correlation underestimates the actual pressure of GLC samples as it does not take elasticity effects into account.

5. Energy Analysis of Graphene-Encapsulated Water

Although extreme pressures inside enclosures of nanometer-thick graphene layers appear to be eccentric, such values have been physically and mathematically justified. Khetonesa et al.[16] have analyzed the energy components playing a role in the pressure buildup in graphene enclosures on a solid substrate. The shape and the pressure of graphene bubbles on a solid substrate were stabilized in equilibrium conditions formed between graphene layers, the solid substrate, and the enclosure content. Thus, the energy inside each graphene enclosure was modeled by three main components: 1) graphene–graphene and graphene–liquid interactions, 2) graphene elasticity, and 3) internal energy of the content. Herein, applying the same approach, we have modeled each GLC with respect to its geometry and energy components. Assuming isothermal conditions, the pressure buildup inside each GLC was modeled as the product of energy spent in the GLC fabrication procedure. In our model, GLCs are formed upon squeezing nanodroplets of water between graphene sheets. The magnitude of GLCs' internal pressure is a function of its size and stems from four main energy components: 1) the adhesion energy between graphene layers (E_{VdW}), 2) the adhesion energy between graphene and water ($E_{Laplace}$), 3) the elasticity energy of graphene substrate (E_{el}), and 4) the internal energy of water (E_l). E_{VdW} is the energy spent to peel adjacent graphene layers and keep them apart. Second comes the interfacial energy between graphene sheet and water ($E_{Laplace}$), which contributes to the final pressure of the sample. Our calculations show that the contribution of VdW interactions between water and graphene substrate (disjoining pressure) is negligible in final pressure buildup inside GLCs with thicknesses above 1 nm.[52,53] The E_{el} component is the energy spent to bend graphene sheets around water nanodroplets and

keep them askew. Lastly, E_l is the elevation of water nanodroplet internal energy upon encapsulation between graphene sheets. Assuming the initial energy state of water and graphene sheets at zero, the final energy of the system could be written as:

$$E_{tot} = E_{VdW} + E_{Laplace} + E_{el} + E_l\,(V) \tag{11}$$

The VdW energy stems from close contact of graphene sheets and only acts on the footprint of the GLC, which could be estimated as $\gamma_{GG}S_{foot}$, where γ_{GG} is the graphene adhesion energy (120 mJ m^{-2}) and S_{foot} is the GLC footprint. The Laplace energy component is the result of nanoscale interaction of water and graphene which applies on the surface of the graphene exposed to water $\gamma_{GW}S_t$, where γ_{GW} is the adhesion energy of water–graphene and S_t is the total area of graphene exposed to water inside the GLC. The elasticity component of energy is derived based on first order Hooke's law $\frac{1}{2l}YS_{foot}\Delta l^2$ where Y is graphene's young modulus (50–100 MPa)[54–56] and Δl is graphene's strain upon GLC fabrication. The internal energy of water rises as it gets squeezed between graphene sheets. While the temperature variation of GLC is negligible, the pressure of water content is:

$$P = -\left(\frac{\partial E_l}{\partial V_t}\right)_T = -\left(\frac{\partial E_l}{\partial t_{max}}\right)\left(\frac{\partial t_{max}}{\partial V_t}\right) \tag{12}$$

By replacing all the components in Equation (11) we obtain:

$$E_{tot} = \frac{1}{4}\gamma_{GG}l^2\pi + \frac{1}{4}\pi lY\left(\pi\sqrt{\frac{l^2+t_{max}^2}{8}} - l\right)^2 + 4\pi\gamma_{GW}\left(\frac{(l/2)^{3.2} + \left(\frac{1}{2}t_{max}l\right)^{1.6}}{3}\right)^{0.6} - \frac{1}{6}\pi l^2 t_{max}P \tag{13}$$

$$\frac{dE_{tot}}{dt_{max}} = 0 \tag{14}$$

The GLCs are assumed to have a simple ellipsoidal geometry based on previously reported AFM results[16] and our STEM observations, with basal length of l and maximum height of t_{max}:

$$S_t = 4\pi\left(\frac{(l/2)^{3.2} + \left(\frac{1}{2}t_{max}l\right)^{1.6}}{3}\right)^{0.6}$$
$$S_{foot} = \frac{1}{4}\pi l^2 \tag{15}$$
$$V_t = \frac{1}{6}\pi l^2 t_{max}$$

Figure 4 breaks down the total pressure buildup inside GLCs to their three main energy components with respect to the maximum GLC thickness (t_{max}). The pressure buildup resulting from graphene–graphene VdW interactions (Figure 4a) and elasticity component (Figure 4b) constitute the major portion of final pressure of GLCs while the Laplace pressure is responsible for the remainder of the final pressure (Figure 4c). The pressure resulting from VdW interactions of graphene layers have a Laplace nature and vary as $\frac{1}{t_{max}}$. On the other hand, the elasticity component of the total pressure is only a function of l and irrespective of t_{max}. Different pressure components in Figure 4 are sketched for four different aspect ratio values (α) where $\alpha = \frac{l}{t_{max}}$. The aspect ratio was shown to be universal and a function of GLC basal length (l).[16] For instance, it has been shown that for graphene enclosures on solid substrates with l = 200 nm, α oscillates around 10.[16] While the Laplace and VdW terms of the final pressure are mostly similar for different aspect ratio values, the elasticity component increases dramatically in higher α values. The analytical total pressure inside GLC for t_{max} around 10 nm could reach up to 200 MPa, which is in the same order of magnitude as our experimental results. It is evident from Figure 4d that the total pressure inside water GLC approaches infinity, irrespective of α, when t_{max} drops below 1 nm, which is well expected from the Laplace pressure correlation $\left(\Delta P = \frac{2\gamma}{R}\right)$.

Equations (13)–(15) are derived considering some geometrical assumptions based on previously published articles.[6,16] The energy analysis above idealizes the GLC to a symmetric ellipsoid capsule with $l/2$, $l/2$ and $t_{max}/2$ axes. For the GLCs with different geometries (spherical, octahedral, flat, etc.), Equations (13) and (15) should be revised. For instance, in Figure S9, Supporting Information, we have analyzed a GLC with triangular-base hexahedral geometry. It would be interesting for future studies to investigate the pressure buildup inside GLCs with different geometries, both experimentally and analytically. As a rule of thumb, in the GLC capsules the internal pressure decreases as the maximum thickness of the sample (t_{max}) increases, to the extent that for samples as thick as 1 µm (encapsulated cells, bacteria, etc.), it is safe to assume the specimen is under atmospheric pressure.

The radiolysis and electron dose effect on the state of water molecules are also very important in liquid-cell TEM.[57,58] During radiolysis, the electron beam undergoes inelastic scattering events in water, resulting in the dissociation of a number of water molecules and the release of radicals (mostly hydroxyl groups).[58,59] While water is susceptible to radiolysis, reducing the electron beam intensity and the number of electron scattering events also minimizes the concentration of dissolved electrons and radicals that may affect the equilibrium condition in the nanoenvironment of GLCs.[45] Under equilibrium conditions, the radiolysis byproducts recombine and neutralize the liquid environment, which in turn minimizes the complicating effects of radiolysis.[57] Herein, after confirming the existence of water within our GLCs (Figure S7, Supporting Information), STEM observations were performed under low beam currents. The electron beam dose rate during our EELS analysis was estimated to be around 0.3 e Å^{-2}s^{-1}, which is well below the intensity threshold of water dissociation (6–9 e Å^{-2}s^{-1}).[26,45] Figure S10, Supporting Information, depicts a specimen after successive spot EELS measurements. The stability of the liquid-free portion of the GLC confirms the resilience of this sample in the low dose-rate electron beam condition, and confirms our assertion that radiolysis did not play a significant role in the present tests. There are also other

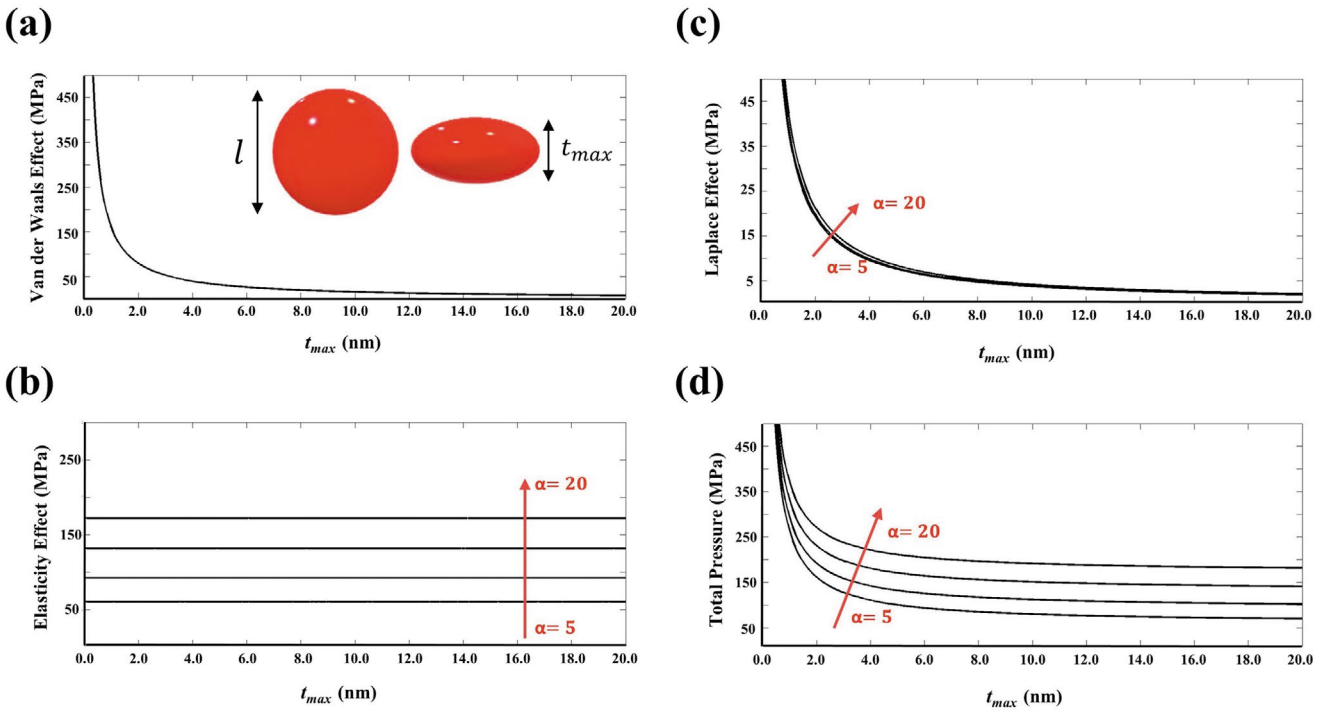

Figure 4. Analytical pressure estimates inside water GLCs with respect to cell enclosure height t_{max} and different values of aspect ratio α. a) The Van der Waals (VdW) pressure stems from the substantial adhesion energy between the graphene layers. The VdW pressure varies as $1/t_{max}$. b) Keeping layers of graphene bent around the water sample stores energy in the water film, which in turn increases the pressure of the GLC. However, the elasticity pressure is only a function of l and does not change with t_{max}. c) The Laplace pressure is a result of adhesion energy between water and graphene layers of the GLC. The magnitude of Laplace pressure varies as $1/t_{max}$ as expected. d) The total pressure inside the GLC is the sum of the three pressures shown in a–c.

sources of uncertainty in our assumptions that need to be addressed. First, while Egerton's free electron model works best for metals and semiconductors, it deviates slightly for insulating materials including water. This issue was addressed by applying high electron acceleration energies (200 keV) to overcome the Fermi level. Next, the deconvolution of water EELS signal from that of Si_3N_4 in liquid flow holder and graphene could introduce errors to these calculations. For this work, the deconvolution algorithm was applied uniformly to all spectra in both systems.

In order to describe microscopic conditions in GLCs of different sizes, we modeled these systems by atomistic molecular dynamics simulations. In earlier studies, we have shown that water nanodroplets can fold graphene into different superstructures to form GLCs.[60] Here, we ran molecular dynamic simulations on two type of GLCs with: 1) square graphene sheets (60×60 nm^2) and 2) circular graphene sheets with a radius of 30 nm. Each type of GLC was simulated with different numbers of water molecules, ranging from 2.5×10^4 to 3.2×10^5 molecules. We calculated the densities of each system in order to determine its pressure. In all GLC systems shown in Figures S11 and S12, Supporting Information, we determined the radial profile of water density (see methods for further details). In order to assess the density vs. pressure in bulk water and benchmark these densities with our GLC calculations, we did the same type of calculations in bulk water (without the GLC) at pressures of 0.101325, 10.325, and 30.3975 MPa, shown in Figure S13, Supporting Information. From these dependencies on the known applied pressures, we have determined density vs pressure for water in an arbitrary environment, $\left(\frac{\partial \rho}{\partial p}\right)_T \approx 5.9 \times 10^{-4}$ g MPa^{-1} cm^{-3}, as shown in Figure 5c (inset). This benchmarking allows us to determine the pressures inside GLCs from the water densities within them.

Figure 5c shows the calculated pressures based on the densities of water in GLCs as a function of the number of entrapped water molecules. The deviation of density ($\Delta\rho$) from the ambient density (1 g cm^{-3}) and the pressure of water droplet in the GLCs are inversely proportional to the number of water molecules confined inside each GLC. The densities and shapes of the cavities of GLCs formed with either square or circular graphene with the same number of entrapped water molecules are very similar (Figures S11 and S12, Supporting Information). The significantly lower pressure of water in Figure 5c for the square GLC with 0.6×10^5 water molecules is an outlier and could be the result of high simulation uncertainty when calculating the radial profile of water density in that GLC (Figure S11c, Supporting Information). In order to determine the contribution of Laplace pressure in the pressure build-up in the GLC-encapsulated water, the Laplace pressures of free water droplets containing the same number of water molecules in each GLC were calculated (Figure 5c). The calculated Laplace pressure in the free water droplets constitute ≈25–33% of the final pressure in each GLC, while graphene-graphene VdW interactions and the graphene elasticity component make up the rest.

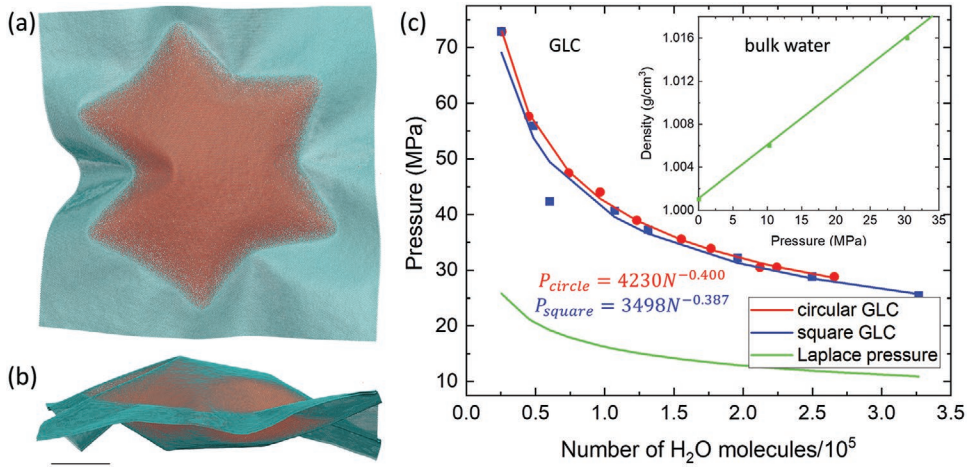

Figure 5. a) Top, and b) side views of a GLC with square graphene containing 3.2×10^5 water molecules. Scale bar denotes 10 nm. c) Water pressure in GLCs with square and circular graphene sheets vs. number of entrapped water molecules. The red and blue lines are fitted pressure curves for the number of water molecules enclosed in each circular and square GLC. The green line represents the Laplace pressure inside free water droplets containing the same number of water molecules as the GLCs. The inset is a scatter graph of densities of bulk water with respect to pressure.

In summary, the density and pressure of water entrapped between sheets of graphene were measured using low-loss EELS, and validated by energy conservation models and molecular dynamics simulations. The density of water in the GLC was derived using the free electron model and was correlated to the pressure of water in the GLC system. The density of water in the GLC sample with basal length of 200 nm reached 1.12 ± 0.10 g cm^{-3} indicating that the internal pressure of GLC was up to 400 ± 50 MPa. To evaluate our experimental results, an energy conservation method was applied on water within GLCs. The total pressure buildup in water upon GLC fabrication was determined from three main components of pressure: Laplace, VdW, and elasticity effects. It was concluded that graphene elasticity and interlayer VdW interactions have the most significant contribution on the pressure buildup inside relatively large graphene enclosures. Finally, our atomistic molecular dynamic simulations revealed the density and pressure of graphene-enclosed water with respect to the number of encased water molecules in GLCs featuring square or circular geometries. The present work offers new insight on the thermodynamic state of water under graphene encasement, and opens new opportunities for examination of liquid specimens under confinement using advanced TEM and EELS techniques.

6. Methods

Graphene crystals were grown using previously-developed protocols for low pressure chemical vapor deposition (LPCVD).[61] Copper was annealed inside the LPCVD tube for 30 min prior to graphene growth. Then hydrogen and methane gases were flowed in the tube with flow rate of 7.0 and 5.0 standard cubic centimeters per minute (SCCM), respectively, at the operating temperature of 1000 °C. Graphene was grown on copper substrates and transferred to TEM grids after etching and washing steps.[27] Graphene–copper substrates were kept afloat on the ammonium persulfate (APS) solution for 3 h to etch the copper layer. Free floating graphene was then carefully transferred on deionized (D.I.) water with the assistance of a microscope slide to wash off the etchant residue. The graphene layer was scooped by a 2000 mesh TEM grid to form graphene-coated grids. APS and biological-grade D.I. water were purchased from Sigma-Aldrich. After the deposition of D.I. water volumes on the graphene side of the TEM grid, a second graphene layer was scooped up to seal water between the graphene-coated grid and the second layer of graphene (Figure S1, Supporting Information). The grid was left in the desiccator overnight to evaporate any excess amount of water and form GLCs on the TEM grid. The Poseidon liquid flow holder and E-Chips Poseidon 210 were purchased from Protochips. Prior to microscopy, silicon chips were washed in acetone and ethanol for 3 min subsequently and air dried. Then chips were plasma-treated for 1 min. Chips were then assembled on the liquid flow holder and kept in dry station vacuum to check for cracks on their Si_3N_4 windows. The assembled holder was then inserted in the microscope for further microscopy and EELS experiments. Electron microscopy of water in the liquid flow holder and GLC was carried out in the aberration-corrected JEOL ARM-200F operating at 200 keV, respectively, with the beam current of 5 μA at the gun. Analytical EELS measurements on water were carried out using Gatan Quantum GIF with channel intervals of 0.15 eV. The beam intensity on the sample was calculated to be 0.3 e Å^{-2} s^{-1}, which is well below the water dissociation threshold.[45]

The MD simulations were performed with the NAMD 2.13 package[62], using a CHARMM 27 force field[63] for graphene. The TIP3P model was used for water molecules. The simulations were described by a Langevin dynamics in a NVT ensemble for systems with GLC and $T = 310$ K, where V varied according to number of water molecules, and NPT ensemble for bulk water system, with $p = 1$, 100, 300 atm and $T = 310$ K. A Particle Mesh Ewald[64] summation was used to calculate long-range Coulombic interactions, with a grid spacing of 1.0. Short-range dispersion interactions used a switching algorithm, with an

on–off distance of 10/12 Å. Pairlists were recorded for atoms 13.5 Å apart, updated every 20 steps; 1–4 interactions were not scaled.

Bulk water simulations had 133 050 water molecules. GLC systems have only two graphene sheets, modeled as structure of neutral carbon atoms, with no terminal hydrogen atoms. Constraints for preparation, minimization, pre-equilibration, and production runs of the system were only applied to atoms within 5 Å from the edges, restrained harmonically in the z direction only. GLC systems were prepared by selecting carbon atoms which were within 10 nm from the center and pulling them apart in the z direction. Each GLC had different-sized cavities. Ellipsoid shaped solvation boxes were placed in the cavities between the graphene sheets. The periodic boundary condition was set up such that, in the xy directions, the graphene surfaces in the principal box were 1 nm away from the box. In the z-direction, the graphene surfaces were separated by 50% above the dimensions of the ellipsoidal water droplet, to minimize interactions. Both types of systems were minimized for 5000 steps and pre-equilibrated for 0.100 ns. Bulk water systems had 2 ns of production runs, whereas GLC systems had 10 ns of production runs. Coordinates were recorded every 10 ps.

The water densities in different systems were determined from a calculation of the radial dependence of the number of water molecules within concentric spheres. We took concentric spheres of a different diameter, r (starting at r = 5Å), and increments of 1–5 Å, until the maximum height of graphene was reached for the entire simulation. We calculated the mass of all water atoms within the sphere. At each value of r, we determined the average density and its standard deviation, integrated with respect to time. From the standard deviations, we determined the uncertainty at the 99.5% confidence level. We estimated the value of the density, using the density values at intermediate values of r, which were consistent with each other and had low uncertainty. When r was too small, the uncertainty was large; when r was too large, the density could be underestimated, because the volume could include regions outside the GLC, which was vacuum.

Supporting Information

Supporting Information is available from the Wiley Online Library or from the author.

Acknowledgements

T.S. acknowledges funding from NSF-CBET Awards 1803693 and 1805753. R.S.-Y. is thankful for NSF-DMR Award 1710049. C.M.M. acknowledges support from NSF-CBET Award 1805753.

Conflict of Interest

The authors declare no conflict of interest.

Authors Contributions

The project idea was conceived by S.M.G., R.S.-Y., C.M.M., and T.S. All graphene liquid cells and liquid flow holder samples were fabricated by S.M.G. The STEM and EELS analysis as well as pressure analysis were performed by S.M.G. who also developed the energy analysis on water entrapped between graphene layers. S.M.G. and P.K. wrote the manuscript, and all authors read and commented on the manuscript.

Keywords

confined liquids, graphene liquid cells, pressure, transmission electron microscopy

Received: October 11, 2019
Revised: March 7, 2020
Published online:

[1] G. F. Audette, E. J. van Schaik, B. Hazes, R. T. Irvin, *Nano Lett.* **2004**, *4*, 1897.
[2] S. Gravelle, L. Joly, F. Detcheverry, C. Ybert, C. Cottin-Bizonne, L. Bocquet, *Proc. Natl. Acad. Sci. USA* **2013**, *110*, 16367.
[3] J. C. Rasaiah, S. Garde, G. Hummer, *Annu. Rev. Phys. Chem.* **2008**, *59*, 713.
[4] J. N. Israelachvili, R. M. Pashley, *Nature* **1983**, *306*, 249.
[5] S. M. Ghodsi, C. M. Megaridis, R. Shahbazian-Yassar, T. Shokuhfar, *Small Methods* **2019**, *3*, 1900026
[6] S. M. Ghodsi, S. Anand, R. Shahbazian-Yassar, T. Shokuhfar, C. M. Megaridis, *ACS Nano* **2019**, *13*, 4677.
[7] C. H. Y. X. Lim, A. Sorkin, Q. Bao, A. Li, K. Zhang, M. Nesladek, K. P. Loh, *Nat. Commun.* **2013**, *4*, 1556.
[8] W. Zhou, K. Yin, C. Wang, Y. Zhang, T. Xu, A. Borisevich, L. Sun, J. C. Idrobo, M. F. Chisholm, S. T. Pantelides, R. F. Klie, A. R. Lupini, *Nature* **2015**, *528*, E1.
[9] G. Algara-Siller, O. Lehtinen, F. C. Wang, R. R. Nair, U. Kaiser, H. A. Wu, A. K. Geim, I. V. Grigorieva, *Nature* **2015**, *519*, 443.
[10] R. Zangi, *J. Phys. Condens. Matter* **2004**, *16*, S5371.
[11] J. C. Johnston, N. Kastelowitz, V. Molinero, *J. Chem. Phys.* **2010**, *133*, 154516.
[12] X. Feng, S. Maier, M. Salmeron, *J. Am. Chem. Soc.* **2012**, *134*, 5662.
[13] K. T. He, J. D. Wood, G. P. Doidge, E. Pop, J. W. Lyding, *Nano Lett.* **2012**, *12*, 2665.
[14] K. S. Vasu, E. Prestat, J. Abraham, J. Dix, R. J. Kashtiban, J. Beheshtian, J. Sloan, P. Carbone, M. Neek-Amal, S. J. Haigh, A. K. Geim, R. R. Nair, *Nat. Commun.* **2016**, *7*, 12168.
[15] C. H. Y. X. Lim, M. Nesladek, K. P. Loh, *Angew. Chem., Int. Ed.* **2014**, *53*, 215.
[16] E. Khestanova, F. Guinea, L. Fumagalli, A. K. Geim, I. V. Grigorieva, *Nat. Commun.* **2016**, *7*, 12587.
[17] J. Wu, W. Gao, H. Yang, J.-M. Zuo, *Microsc. Microanal.* **2014**, *20*, 1508.
[18] J. Y. Cheong, J. H. Chang, H. K. Seo, J. M. Yuk, J. W. Shin, J. Y. Lee, I.-D. Kim, *Nano Energy* **2016**, *25*, 154.
[19] J. P. Patterson, P. Abellan Baeza, M. Denny, S. Cohen, C. Park, N. D. Browning, J. E. Evans, N. C. Gianneschi, *Microsc. Microanal.* **2013**, *20*, 1614.
[20] A. De Clercq, W. Dachraoui, O. Margeat, K. Pelzer, C. R. Henry, S. Giorgio, *J. Phys. Chem. Lett.* **2014**, *5*, 2126.
[21] V. Berry, *Carbon* **2013**, *62*, 1.
[22] S. Deng, V. Berry, *Mater. Today* **2016**, *19*, 197.
[23] K. Sotthewes, P. Bampoulis, H. J. W. Zandvliet, D. Lohse, B. Poelsema, *ACS Nano* **2017**, *11*, 12723.
[24] N. Mohanty, V. Berry, *Nano Lett.* **2008**, *8*, 4469.
[25] K. Xu, P. Cao, J. R. Heath, *Science* **2010**, *329*, 1188.
[26] C. Wang, Q. Qiao, T. Shokuhfar, R. F. Klie, *Adv. Mater.* **2014**, *26*, 3410.
[27] A. R. Ribeiro, A. Mukherjee, X. Hu, S. Shafien, R. Ghodsi, K. He, S. Gemini-Piperni, C. Wang, R. F. Klie, T. Shokuhfar,

R. Shahbazian-Yassar, R. Borojevic, L. A. Rocha, J. M. Granjeiro, *Nanoscale* **2017**, *9*, 10684.
[28] J. F. Creemer, S. Helveg, G. H. Hoveling, S. Ullmann, A. M. Molenbroek, P. M. Sarro, H. W. Zandbergen, *Ultramicroscopy* **2008**, *108*, 993.
[29] N. D. Jonge, D. B. Peckys, G. J. Kremers, D. W. Piston, *Proc. Natl. Acad. Sci. USA* **2009**, *106*, 2159.
[30] X. Chen, C. Li, H. Cao, *Nanoscale* **2015**, *7*, 4811.
[31] E. Firlar, M. Ouy, L. Covnot, Y. Xing, D. Lee, A. Chan, Y. He, B. Song, S. Afelik, Y. Wang, R. Shahbazian-Yassar, J. Oberholzer, T. Shokuhfar, *Int. J. Nanomed.* **2019**, *14*, 371.
[32] E. Firlar, M. Ouy, A. Bogdanowicz, L. Covnot, B. Song, Y. Nadkarni, R. Shahbazian-Yassar, T. Shokuhfar, *Nanoscale* **2019**, *11*, 698.
[33] X. Li, C. W. Magnuson, A. Venugopal, R. M. Tromp, J. B. Hannon, E. M. Vogel, L. Colombo, R. S. Ruoff, *J. Am. Chem. Soc.* **2011**, *133*, 2816.
[34] K. L. Jungjohann, J. E. Evans, J. A. Aguiar, I. Arslan, N. D. Browning, *Microsc. Microanal.* **2012**, *18*, 621.
[35] T. Malis, S. C. Cheng, R. F. Egerton, *J. Electron Microsc. Tech.* **1988**, *8*, 193.
[36] Y. Sasaki, R. Kitaura, J. M. Yuk, A. Zettl, H. Shinohara, *Chem. Phys. Lett.* **2016**, *650*, 107.
[37] X. Hu, P. Yasaei, J. Jokisaari, S. Öğüt, A. Salehi-Khojin, R. F. Klie, *Phys. Rev. Lett.* **2018**, *120*, 055902.
[38] M. H. Gass, U. Bangert, A. L. Bleloch, P. Wang, R. R. Nair, A. K. Geim, *Nat. Nanotechnol.* **2008**, *3*, 676.
[39] X. Hu, P. Yasaei, J. Jokisaari, S. Öğüt, A. Salehi-Khojin, R. F. Klie, *Phys. Rev. Lett.* **2018**, *120*, 55902.
[40] M. Tanase, J. Winterstein, R. Sharma, V. Aksyuk, G. Holland, J. A. Liddle, *Microsc. Microanal.* **2015**, *21*, 1629.
[41] R. F. Egerton, *Electron Energy-Loss Spectroscopy in the Electron Microscope*, Springer Science & Business Media, Berlin **2011**.
[42] J. Hren, *Introduction to Analytical Electron Microscopy*, Springer Science & Business Media, Berlin **2013**.
[43] M. M. Disko, C. C. Ahn*Transmission Electron Energy Loss Spectrometry in Materials Science*, 2, Minerals, Metals, & Materials Society, Warrendale, PA **1992**.
[44] D. B. Williams, C. B. Carter, in *Transmission Electron Microscopy*, Springer, Berlin **1996**, pp. 3–17.
[45] C. Wang, T. Shokuhfar, R. F. Klie, *Adv. Mater.* **2016**, *28*, 7716.
[46] G. S. Density, *J. Chem. Eng. Data* **1975**, *20*, 97.
[47] F. H. Fisher, O. E. Dial Jr., *Report SIO 75-28, University of California*, San Diego, Marine Physical Laboratory of the Scripps Institution of Oceanography, San Diego, CA **1975**.
[48] J. Chandran R, A. Salih, *Fluid Phase Equilib.* **2019**, *483*, 182.
[49] G. Zamborlini, M. Imam, L. L. Patera, T. O. Menteş, N. Stojić, C. Africh, A. Sala, N. Binggeli, G. Comelli, A. Locatelli, *Nano Lett.* **2015**, *15*, 6162.
[50] D. Shin, J. B. Park, Y.-J. Kim, S. J. Kim, J. H. Kang, B. Lee, S.-P. Cho, B. H. Hong, K. S. Novoselov, *Nat. Commun.* **2015**, *6*, 6068.
[51] J. S Bunch, S. S. Verbridge, J. S. Alden, A. M. van der Zande, J. M. Parpia, H. G. Craighead, P. L. McEuen, *Nano Lett.* **2008**, *8*, 2458.
[52] Y.-C. Chiou, T. A. Olukan, M. A. Almahri, H. Apostoleris, C. H. Chiu, C.-Y. Lai, J.-Y. Lu, S. Santos, I. Almansouri, M. Chiesa, *Langmuir* **2018**, *34*, 12335.
[53] T. Peng, K. Peng, Q. Li, *J. Phys. Chem. C* **2015**, *119*, 14273.
[54] C. Lee, X. Wei, J. W. Kysar, J. Hone, *Science* **2008**, *321*, 385.
[55] C. S. Ruiz-Vargas, H. L. Zhuang, P. Y. Huang, A. M. van der Zande, S. Garg, P. L. McEuen, D. A. Muller, R. G. Hennig, J. Park, *Nano Lett.* **2011**, *11*, 2259.
[56] R. J. T. Nicholl, H. J. Conley, N. V. Lavrik, I. Vlassiouk, Y. S. Puzyrev, V. P. Sreenivas, S. T. Pantelides, K. I. Bolotin, *Nat. Commun.* **2015**, *6*, 8789.
[57] J. A. LaVerne, S. M. Pimblott, *J. Phys. Chem.* **1991**, *95*, 3196.
[58] N. M. Schneider, M. M. Norton, B. J. Mendel, J. M. Grogan, F. M. Ross, H. H. Bau, *J. Phys. Chem. C* **2014**, *118*, 22373.
[59] M. A. Hill, F. A. Smith, *Radiat. Phys. Chem.* **1994**, *43*, 265.
[60] N. Patra, B. Wang, P. Král, *Nano Lett.* **2009**, *9*, 3766.
[61] J. W. Suk, A. Kitt, C. W. Magnuson, Y. Hao, S. Ahmed, J. An, A. K. Swan, B. B. Goldberg, R. S. Ruoff, *ACS Nano* **2011**, *5*, 6916.
[62] J. C. Phillips, R. Braun, W. Wang, J. Gumbart, E. Tajkhorshid, E. Villa, C. Chipot, R. D. Skeel, L. Kalé, K. Schulten, *J. Comput. Chem.* **2005**, *26*, 1781.
[63] M. Ad, N. All, *J. Phys. Chem. B* **1998**, *102*, 3586.
[64] T. Darden, D. York, L. Pedersen, *J. Chem. Phys.* **1993**, *98*, 10089.

